AGU PUBLICATIONS

JGR

Journal of Geophysical Research: Oceans

RESEARCH ARTICLE

10.1002/2016JC012568

Impacts of oil spills on altimeter waveforms and radar backscatter cross section

Yongcun Cheng[1], Jean Tournadre[2], Xiaofeng Li[3], Qing Xu[4], and Bertrand Chapron[2]

[1]Center for Coastal Physical Oceanography, Old Dominion University, Norfolk, Virginia, USA, [2]Laboratoire d'Océanographie Physique et Spatiale, IFREMER, CNRS, Université de Bretagne Occidentale, Plouzané, France, [3]GST, NOAA/NESDIS/STAR, College Park, Maryland, USA, [4]College of Oceanography, Hohai University, Nanjing, China

Key Points:
- Confirmed the impact of oil spills on satellite altimetry measured waveforms
- Quantified the variation of altimetry sigma0 as a function of oil thickness, wind speed, and radar band
- Altimeter data can certainly be used as a complementary data set to validate and delineate thick oil cover

Correspondence to:
Y. Cheng,
y1cheng@odu.edu

Citation:
Cheng, Y., J. Tournadre, X. Li, Q. Xu, and B. Chapron (2017), Impacts of oil spills on altimeter waveforms and radar backscatter cross section, *J. Geophys. Res. Oceans*, *122*, 3621–3637, doi:10.1002/2016JC012568.

Received 21 NOV 2016
Accepted 26 MAR 2017
Accepted article online 4 APR 2017
Published online 2 MAY 2017

Abstract Ocean surface films can damp short capillary-gravity waves, reduce the surface mean square slope, and induce "sigma0 blooms" in satellite altimeter data. No study has ascertained the effect of such film on altimeter measurements due to lack of film data. The availability of Environmental Response Management Application (ERMA) oil cover, daily oil spill extent, and thickness data acquired during the Deepwater Horizon (DWH) oil spill accident provides a unique opportunity to evaluate the impact of surface film on altimeter data. In this study, the Jason-1/2 passes nearest to the DWH platform are analyzed to understand the waveform distortion caused by the spill as well as the variation of σ_0 as a function of oil thickness, wind speed, and radar band. Jason-1/2 Ku-band σ_0 increased by 10 dB at low wind speed (<3 m s^{-1}) in the oil-covered area. The mean σ_0 in Ku and C bands increased by 1.0–3.5 dB for thick oil and 0.9–2.9 dB for thin oil while the waveforms are strongly distorted. As the wind increases up to 6 m s^{-1}, the mean σ_0 bloom and waveform distortion in both Ku and C bands weakened for both thick and thin oil. When wind exceeds 6 m s^{-1}, only does the σ_0 in Ku band slightly increase by 0.2–0.5 dB for thick oil. The study shows that high-resolution altimeter data can certainly help better evaluate the thickness of oil spill, particularly at low wind speeds.

1. Introduction

Geophysical parameter estimates from altimeter can often be degraded by very high surface radar backscattering coefficient (hereafter denoted by backscatter, σ_0), which indicate that the altimeter waveform model used to infer the geophysical parameters [*Brown*, 1977] is no longer valid. Several studies conducted using different altimeter data (Topex, Jason-1, and Envisat) have shown that these events named "sigma0 blooms" affect almost 6% of the measurements over the ocean. The global descriptions of the σ_0 blooms events are most of the time but not always associated with low winds [*Mitchum et al.*, 2004; *Thibaut et al.*, 2007]. It has also been hypothesized that surface slicks could play a significant role in σ_0 blooms. Two studies [*Garcia*, 1999; *Tournadre et al.*, 2006] using analytical models of altimeter waveforms have well reproduced some observed σ_0 blooms for Topex and Jason-1 altimeters. The results demonstrate significant inhomogeneity of the surface backscatter, such as the ones associated with surface slicks, can cause σ_0 bloom events. However, it has not been possible to ascertain the relationship between oil slick and bloom, furthermore, to quantify the effect of oil slick on altimeter measurements, attributed to lacking of reliable surface oil films, information collocated, and coincident with altimeter data.

The Deepwater Horizon (DWH) oil spill event occurred on 20 April 2010. The reviews of the DWH oil spill event can be found in the literature [*Fingas and Brown*, 2014; *Liu et al.*, 2013; *Leifer et al.*, 2012]. It was the largest accidental marine oil spill in the U.S. petroleum industry history. The leak was finally stopped on 15 July 2010. The time-varying oil flow rate was estimated between 53,000 and 63,000 barrels/d [*McNutt et al.*, 2011; *Kourafalou and Androulidakis*, 2013] and the total oil leak was $4.4 \times 10^6 \pm 20\%$ barrels (about 700,000 m^3) [*Crone and Tolstoy*, 2010]. An extensive set of in situ and satellite (Synthetic Aperture Radar (SAR) and radiometers) data have been collected, archived, and distributed. The SAR, Moderate Resolution Imaging Spectroradiometer (MODIS) observations of DWH oil spill have been well documented in the previous studies [e.g., *Bulgarelli and Djavidnia*, 2012; *Garcia-Pineda et al.*, 2013; *Jones et al.*, 2011; *Leifer et al.*, 2012; *Li et al.*, 2013; *Liu et al.*, 2011; *Minchew et al.*, 2012; *Migliaccio and Nunziata*, 2014; *Sun et al.*, 2016]. In particular, all the available SAR and visible images during the spill have been processed to produce daily oil spill

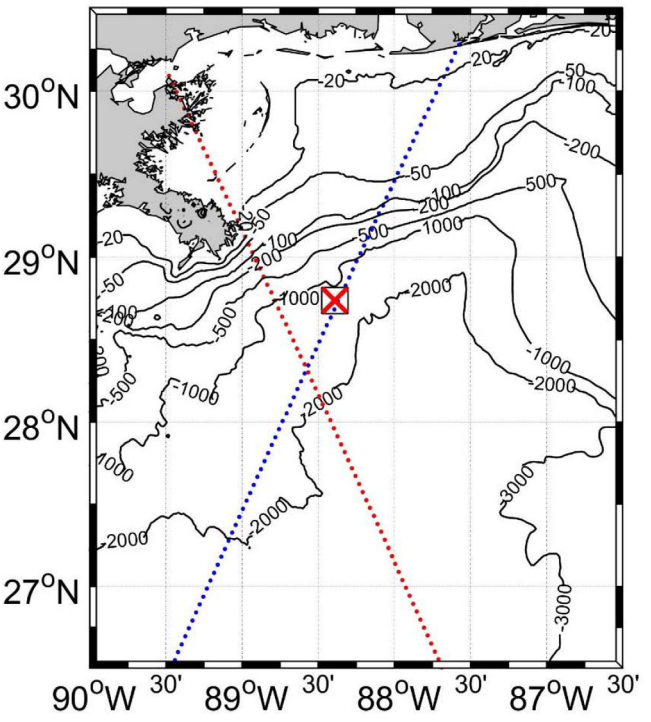

Figure 1. Map and water depth (m) of the Gulf of Mexico and the locations of Jason-1 (blue, pass 015) and Jason-2 (red, pass 204) ground tracks. The location of the "DWH" is marked as a red cross.

extent and thickness fields from 25 April 2010 to 28 July 2010. This unique data set offers a new opportunity to evaluate and quantify the impact of surface film on altimeter data in three aspects. It helps us to first ascertain that surface film does cause σ_0 bloom, and then to analyze the wind condition under which bloom occurs, and finally to quantify the impact of film and its thickness on the measured σ_0.

Two altimeter passes close to the DWH platform are selected (Jason-1 pass 015 and Jason-2 pass 204, Figure 1). As the repeat period of both satellites is 10 days, 10 cycles of data can be analyzed during the 94 days when the DWH oil covered the ocean surface. Since both Jason-1 and Jason-2 altimeters operate at two frequencies: 13.5 GHz (Ku band) and 5.3 GHz (C band), it is also possible to investigate the frequency dependency of film's impact. Envisat altimeter data are not considered in this study because of its longer repeat period of 35 days that limits the number of overpasses.

The paper is organized as follows. Section 2 presents the altimeter data description used in this study and in particular the surface backscatter field computed by inversion of the altimeter waveforms (see Appendix A). The DWH SAR and visible images, oil spill cover, and thickness data are also described in this section. Section 3 shows the analysis of three altimeter passes in presence of oil slick under different wind conditions. Section 4 analyzes all the altimeter data during the oil spill and estimate the mean impact of film as a function of wind speed, oil thickness, and sensor frequency. The results are discussed in section 5.

2. Data

2.1. Altimetry Data

An altimeter is a nadir looking radar that emits short electromagnetic pulses. It measures the backscattered power by the sea surface as a function of time to construct the echo waveform from which the geophysical parameters are estimated. A detailed description of the principles of altimetry is given for example in *Chelton et al*. [2001]. The backscatter coefficient of the waveform can be expressed as a double convolution product of the radar point target response, the flat sea surface response and the joint probability density function of slope and elevation of the sea surface [*Brown*, 1977]. Over an ocean surface, when we assume a Gaussian altimeter pulse, a Gaussian antenna pattern and a Gaussian random distribution of rough-surface specular points, the waveform has a characteristic shape that can be described analytically using the Brown model (see Figure 2).

The altimeter geophysical parameters: epoch (range), surface backscatter, and significant wave height (SWH) are estimated by fitting the theoretical Brown model to the measured waveforms using a maximum likelihood estimator (MLE) [*Barrick and Lipa*, 1985; *Tournadre et al*., 2011]. Two estimators, MLE-3 and MLE-4, are currently used in standard ocean operational processing. Both estimators compute three parameters (epoch, backscatter, and SWH), while the MLE-4 also solves an additional parameter of the off-nadir angle. The dual frequency signal is mainly used for the correction of ionospheric perturbations.

The Jason-1 and Jason-2 Sensor Geophysical Data Record (SGDR) data are available from the AVISO (Archiving, Validation and Interpretation of Satellite Oceanographic Data). The products provide along-track high-

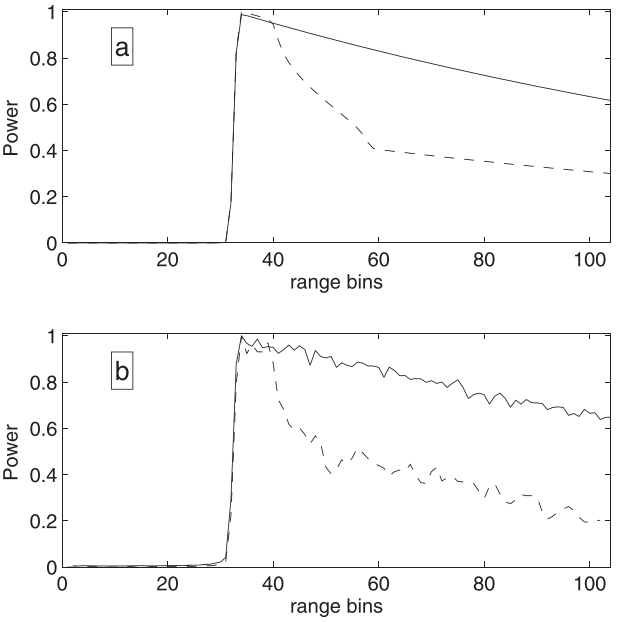

Figure 2. (a) Modeled Jason-2 altimeter waveforms using the Brown model (solid line) and using the *Tournadre et al.* [2006] model in presence of a 5 km circular bright patch of backscatter 5 dB higher than the ocean surface (dashed line). (b) Measured Jason-2 altimeter waveforms for pass 204 cycle 069 at 28°N (solid line) and 28.25°N (dashed line). All waveforms have been scaled by their maximum for a better comparison of their shapes.

rate (20 Hz) Ku-band waveforms as well as the geophysical and environmental parameters. The waveforms are given over 104 temporal bins of width equal to the altimeter pulse length. For Jason-1, σ_0 is estimated using the MLE-4 while the Jason-2 one is estimated using both MLE-3 and MLE-4.

Along with the SGDR, σ_0 at a 290 m resolution over a 8 km wide swath computed by inversion of the waveforms [*Tournadre et al.*, 2011] are also presented. The method is based on the fact that an altimeter can be seen as an imager of the sea surface backscatter whose imaging process is more complex than a classical one in the sense that pixels are not rectangular but annular. The imaging process of the sea surface, i.e., the transform matrix between the real and the waveform spaces, depends only on the satellite and altimeter geometry and can be analytically computed. The pseudo-inverse of the transform matrix can then be used to invert the waveforms in terms of surface backscatter. A more detailed description of the method is given in Appendix A.

2.2. Oil Spill Images and Oil Cover

The DWH oil spill has been well documented and several satellites (especially SAR missions) made daily acquisitions over the Gulf of Mexico during the event. The CSTARS (Center For Southeastern Tropical Advanced Remote Sensing), University of Miami, created the DWH Images database that contains all the SAR and visible images acquired during the oil spill (in general several a day), the NASA (National Aeronautics and Space Administration) Gulf Oil Spill Data, and airborne instrument database. Oil spill leaves a dark feature (e.g., low σ_0) in SAR image [*Buono et al.*, 2016; *Cheng et al.*, 2011; *Liu et al.*, 2010; *Garcia-Pineda et al.*, 2013; *Xu et al.*, 2015; *Nunziata et al.*, 2015]. To confirm the altimeter waveform distortion related to the presence of oil spill, the collected SAR images (Envisat ASAR, Radarsat SAR [*Zhang et al.*, 2011, 2017] and Cosmo-Skymed-1/3 SAR [*Cheng et al.*, 2014]) from these databases have been collocated with the altimeter passes (e.g., within 1 day). The optical sensors such as MODIS show large contrast in sun-glitter imagery for oil spill. A MODIS-Terra image is used to compare with Jason-2 altimeter pass.

During the spill, the Environmental Response Management Application (ERMA) was developed through a joint partnership between National Oceanic and Atmospheric Administration (NOAA) and the University of New Hampshire's Coastal Response Research Center in order to maintain an archive of most of the data from the DWH Response and the Natural Resource Damage Assessment. Among this archive, we use the daily integrated oil cover produced by the U.S. Coast Guard, British Petroleum (BP), and NOAA. It utilized a combination of visual and remote sensing observations from aircraft, as well as satellites (SAR images from various satellites, Landsat Thematic Mapper (TM), NASA's MODIS visible/near infrared (MVIS), and MODIS thermal (MTIR)), to detect the presence of oil in any thickness. The extent of oil on the surface is estimated for each image collected on a given calendar day, classifying the oil into categories based on specific spectral characteristics. The spectral information can be used to estimate an average oil thickness per category. The data are aggregated into the two semiquantitative categories of "thick oil" and "thin oil" to estimate oil coverage on a 5 km $\times$ 5 km grid in the northern Gulf of Mexico and to calculate the percent coverage of thick oil and thin oil per grid cell per day. The data area is available on the ERMA website (https://gomex.erma.noaa.gov/) and the daily oil spill cover were systematically collocated with the altimeter passes.

3. Altimeter Data Analysis

Although SAR is a very powerful tool to operationally detect and monitor oil spill, it lacks of sensitivity to estimate the oil thickness. Its utility for monitoring oil spill trajectories is limited by the satellite revisit time and swath [*Cheng et al*., 2014] and the presence of many "look-alike" oil features in case of very low wind [e.g., *Bao et al*., 2016; *Caruso et al*., 2013; *Kim et al*., 2015; *Li et al*., 2009; *Fiscella et al*., 2000; *Gade et al*., 1998a,1998b]. On the other hand, visible imagery such as MODIS suffers from cloud cover and is limited to day-time observation in sun glint region only [*Hu et al*., 2009; *Xu et al*., 2013; *Zhao et al*., 2014].To illustrate the impact of oil spill on altimeter data and explore the capability of using altimeter data as a complement data set for oil spill monitoring, in particular for low wind condition, we present the analysis of the Jason-2 data along pass 204 from cycles 069 and 072 and Jason-1 data along pass 015 from cycle 306, which correspond to various meteorological situation.

3.1. Jason-2 Pass 204

3.1.1. Low Wind Case

The descending orbit Jason-2 pass 204 enters the Gulf of Mexico around 29.13°N (Figure 1). Figure 3a presents the 20 Hz waveforms along the Jason-2 pass 204 cycle 069 (25 May 2010 06:09 UTC). This case corresponds to a low wind situation for which the mean ECMWF (European Centre for Medium-Range Weather Forecasts) wind speed along the track was 2.9 m s^{-1}. In Figure 3a, the x-label denotes the 104 samples (or range bins) of Jason-2 altimeter waveforms. The onboard tracker normally centers the waveform leading edge at a predefined central gate of 32.5 to keep the waveform well centered in the analysis window [e.g., *Roesler et al*., 2013]. Note that the obvious distortion of the waveforms near 28.25°N and 28.75°N perturbs the onboard tracker and results in the displacement of the leading edge. However, the waveforms leading edge epoch can be repositioned at the nominal central gate of 32.5 by a simple translation using the tracker position information given in the SGDR (Figure 3b) [*Tournadre et al*., 2006]. The C-band waveforms are presented in Figure 3c. They exhibit behaviors very similar to the Ku-band ones.

Figure 3d shows the along-track variations of Ku-band and C-band MLE-3 σ_0 and mean inverted σ_0. In Figure 3d, parabolic shapes are clearly visible in both Ku-band and C-band waveforms near 28.8°N and 28.4°N. The Ku-band MLE-3 σ_0 reaches 20 dB. These shapes result from large variations of backscatter at small scale that distort the waveforms as shown by *Tournadre et al*. [2006]. In Figure 3b, the waveform measured at the center of the parabolic shapes (e.g., at 28.25°N) is different from the waveform measured at 28°N outside the parabolic shapes and follows very well the Brown model (Figure 2a). The waveform shape at 28.25°N is very similar to the one simulated using the *Tournadre et al*. [2006] model for a 5 km radius of 5 dB circular bright patch (Figure 2b).

Tournadre et al. [2009] demonstrated that the square of the off-nadir angle (hereafter denoted by off-nadir angle, ζ), related to the slope of the trailing edge of the waveform, is a very good indicator of the inhomogeneity of the surface backscatter within the altimeter footprint. Figure 4 presents the Ku-band ζ estimated by the MLE-4 estimator and given in the SGDR. The ζ estimated by the linear regression of Ku-band waveform trailing edge is also presented in the figure. Between 28°N and 29°N, ζ anomalously oscillates and reaches very large values (positive and negative). The distortion is remarkable near 28.3°N and responsible for the MLE-4 estimator failure (data missing). The ζ oscillations near 28.3°N and 28.6°N are typical of the presence of surface slicks and coincident to that described by *Tournadre et al*. [2006].

Figures 5a and 5b present the inverted surface Ku-band and C-band σ_0 at 290 m resolution, respectively. In Figure 5b, the ERMA thin and thick oil cover are overlaid. Because of the altimeter sampling geometry, two symmetrical points with respect to the satellite track have identical images in the waveform space leading to a left/right ambiguity. The inverted σ_0 is thus the mean of symmetrical points to the left and the right of the ground track. The inverted fields are plotted on both the left and the right of the satellite track. Figures 5c and 5d show the two collocated SAR images obtained with the closest time to altimeter measurements, e.g., Envisat (25 May 2010 15:47 UTC) and Cosmo-Skymed-3 (25 May 2010 11:57 UTC), respectively. The dark features (low σ_0) that denote the regions affected by oil spill appear very homogeneous with little backscatter variations. The figures clearly show that the presence of oil corresponds to increased surface σ_0 in both Ku and C bands. Near 28°N, in thin oil, the σ_0 increase is limited to about 0.5 dB, but it then grows to almost 10 dB near 28.3°N and 28.6°N where thick oil was detected by ERMA. Within the region of thick oil cover, the surface σ_0 reveals the presence of two very bright patches: a linear one around 28.8°N and a roughly

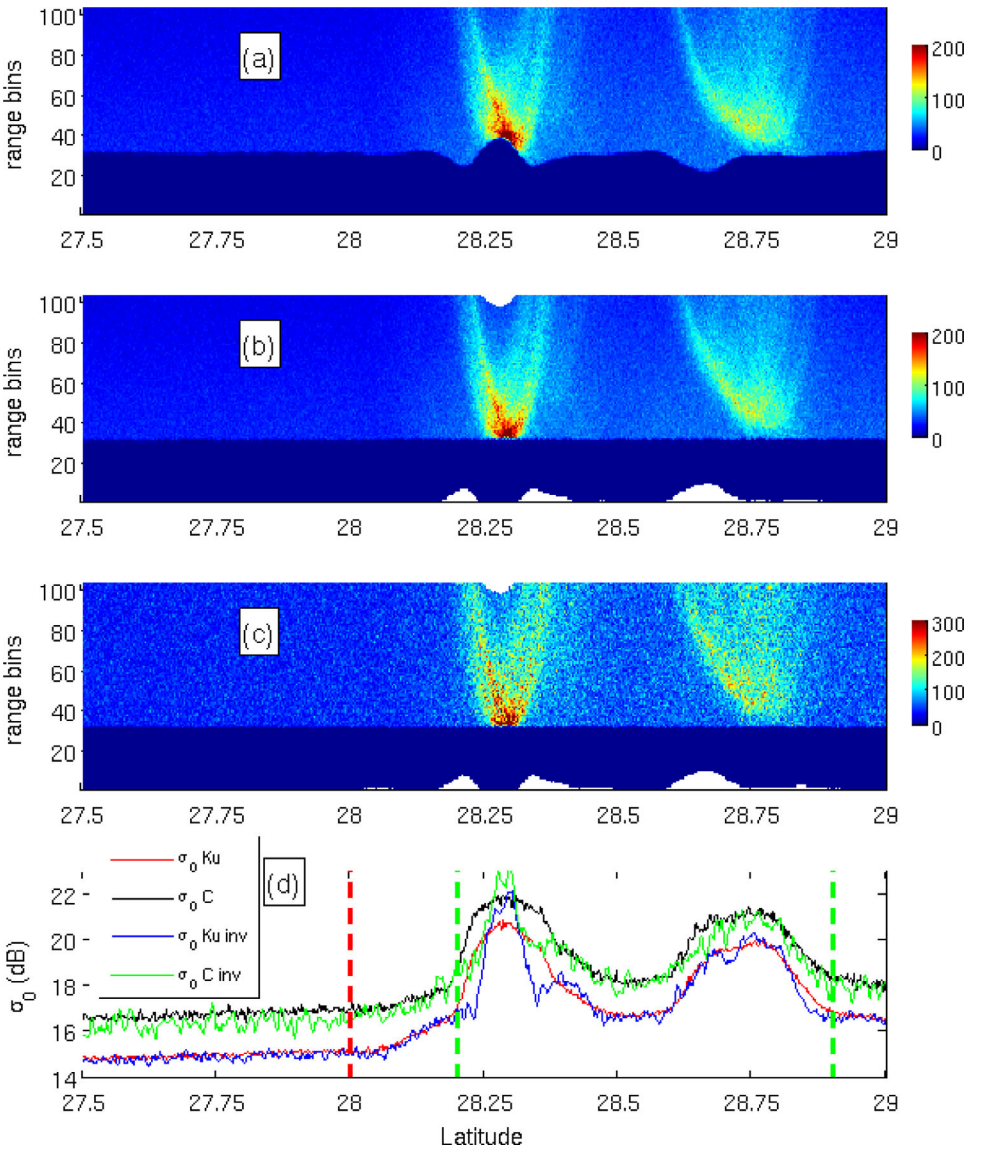

Figure 3. (a) Measured Jason-2 Ku-band waveforms for pass 204 cycle 069. Repositioned (b) Ku-band and (c) C-band waveforms. The color scale represents linear backscatted waveform power. (d) Ku-band and C-band MLE-3 σ_0 (red and black lines) and mean along-track inverted Ku-band and C-band backscatter (blue and green lines). Note that there is a typical difference (~2 dB) between σ_0 values from Ku-bands and C-bands. The dashed green and red line represent the limits of the thin and thick oil cover within the altimeter swath.

circular one near 28.3°N. They correspond to a very strong attenuation of the surface wave that is associated with thicker oil.

3.1.2. Moderate Wind Case

The second example, pass 204 cycle 073 (3 July 2010 21:45 UTC) concerns a case of moderate ECMWF wind of 8.7 m s^{-1}. The repositioned along-track Ku-band and C-band waveforms, the off-nadir angle, and the Ku-band and C-band MLE-3 and inverted σ_0 are presented in Figure 6. The MODIS Terra images (4 July 2010 16:40 UTC, Figure 7c) and Cosmo-Skymed-1 SAR image (3 July 2010 11:56 UTC, Figure 7d) as well as the oil cover ERMA analysis (Figure 7b) are presented in Figure 7. In Figure 7c, the oil spill is clearly visible within the sun glint region but cannot be distinguished from background outside. The SAR image (Figure 7d) captures well the extent of the oil spill but as in Figure 5 there is very little backscatter variability within the dark patch. In Figures 7a and 7b, it can be seen that the impact of oil on altimeter data is more limited than that at low wind (Figures 3 and 4). At C band, both waveforms and σ_0 do not exhibit significant along track variation. At Ku band, a light parabolic shape can be detected near 28.75°N where the ERMA analysis shows

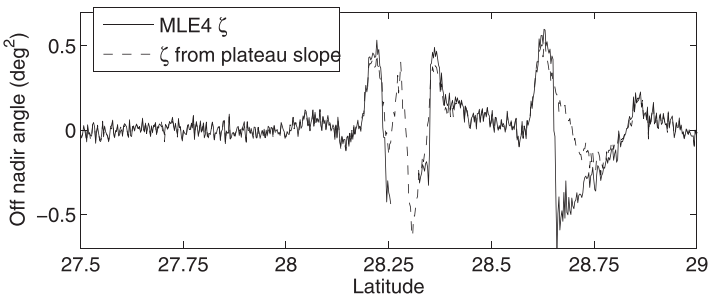

Figure 4. Off-nadir angles for pass 204 cycle 069 from the MLE-4 estimator (solid line) and inferred from the waveforms plateau slope (dashed line).

the presence of thick oil (Figure 7b). It is associated with a local σ_0 increase of some tenth of dB (0.7 dB) and an oscillation of ζ (Figure 6c). The inverted σ_0 presented in Figure 7 shows that this parabolic feature corresponds to patch of enhanced surface backscatter of 1–2 dB. The inverted field also reveals another zone of locally enhanced (0.5 dB) backscatter near 28.6°N in the ERMA thin oil region. It could be associated with thick oil as shown in the Cosmo-Skymed-1 SAR image. Note that the local σ_0 increase within oil are of the same order of magnitude as some local maximums observed near 28.2°N, which are clearly related to wind variability.

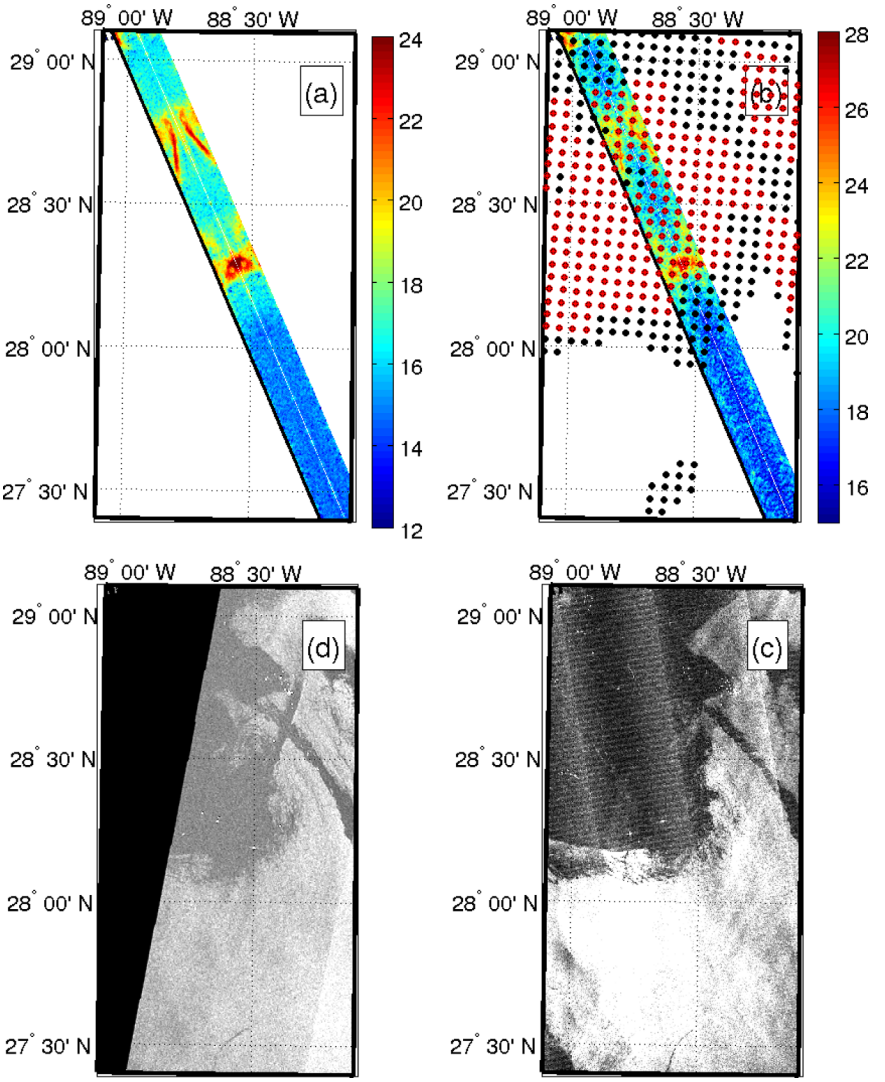

Figure 5. Inverted high-resolution (a) Ku-band and (b) C-band σ_0 (in dB) for Jason-2 pass 204 cycle 069 (25 May 2010 06:09 UTC). The black and red dots in Figure 5b represent the ERMA thin and thick oil cover respectively. (c) Envisat ASAR image (25 May 2010 15:47 UTC). (d) Cosmo-Skymed-3 SAR image (25 May 2010 11:57 UTC).

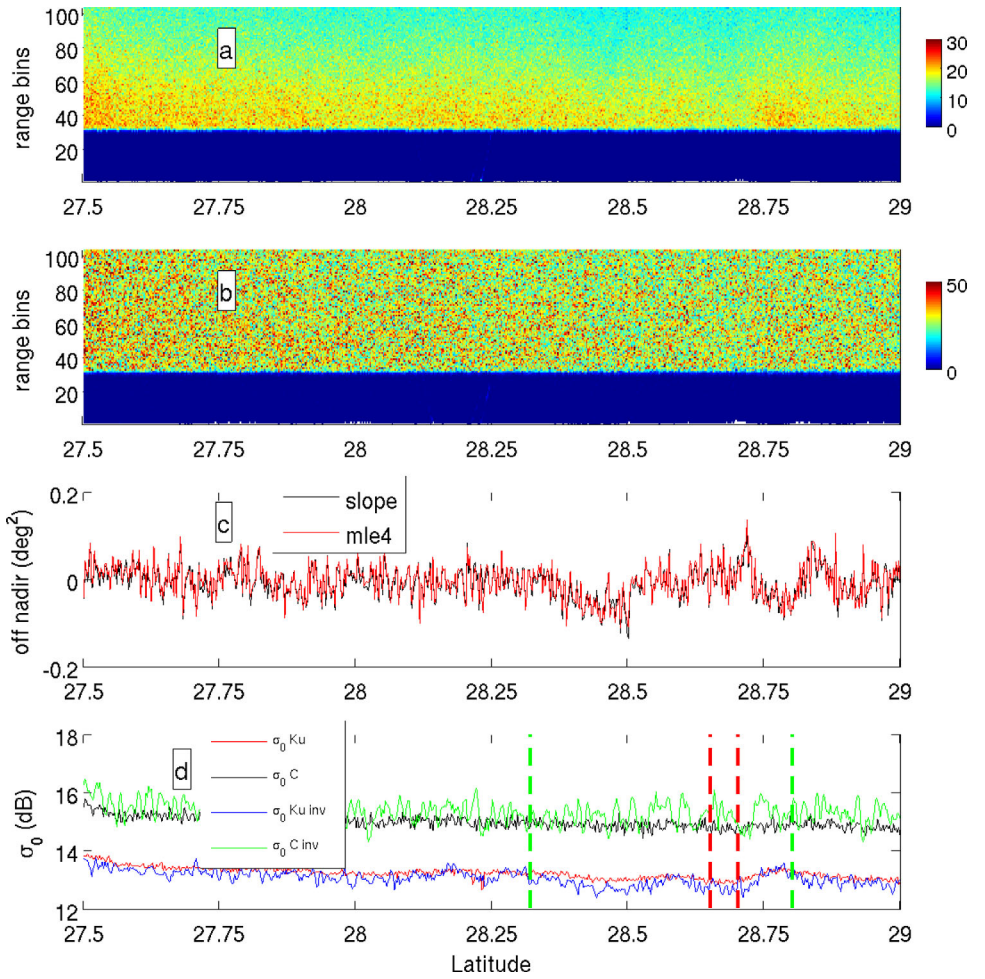

Figure 6. Repositioned Jason-2 (a) Ku-band and (b) C-band waveforms for pass 204 cycle 073 (3 July 2010 21:45 UTC). The color scale represents linear backscatted waveform power. (c) Off-nadir angles from the MLE-4 estimator (red line) and inferred from the waveforms plateau slope (black line). (d) Ku and C-band MLE-3 backscatter (red and black lines) and mean along-track inverted Ku-band and C-band backscatter (blue and green lines). The dashed green and red line represent the limits of the thin and thick oil cover within the altimeter swath.

3.2. Jason-1 Pass 015

The main difference between the two Jason altimeters is that the raw waveform data telemetered from Jason-1 used some, but not all, bin averaging in the trailing edge (bin 64–104) to reduce throughput, whereas all 104 waveform bins are transmitted for Jason-2 [*Thibaut et al.*, 2004]. Unlike Jason-2, the noise level of the Jason-1 decompressed trailing edge data, which affects the noise on the inverted σ_0. On the another hand, compared with Jason-2, only the MLE-4 geophysical parameters are available in the Jason-1 SGDR.

Figures 8a–8d present the Jason-1 pass 015 (ascending orbit) cycle 310 (1 June 2010 18:45 UTC) repositioned Ku-band and C-band waveforms, off-nadir angle and MLE-4 and inverted σ_0. The pass corresponds to a very low wind speed (mean ECMWF wind of 1.9 m s^{-1}) situation and a large ERMA thick oil cover (Figure 9b) as shown on the Radarsat-1 and −2 images (Figures 9c and 9d) taken on the same day at 23:58 and 12:01 UTC, respectively. Compared with dark features in Figures 9c and 9d, Ku-band and C-band waveforms are obviously strongly distorted (Figures 8a and 8b) between 27.5°N and 29.5°N. Several parabolic shapes of different intensity can be seen at 27.75°N, 28.3°N, 28.6°N, 28.8°N, 29.2°N, and 29.5°N. Within these parabolic shapes, ζ oscillates and sometimes exceeds 0.5 deg^2 leading to the failure of the MLE-4 estimator and data missing. The waveform distortion responsible to the MLE-4 Ku-band σ_0 oscillates within the parabolic shapes due to the impact of ζ on σ_0 with the estimator.

The inverted high-resolution Ku-band and C-band σ_0 and collocated Radarsat-1/2 images are shown in Figure 9. There is a very good overall agreement between the ERMA oil extent and the region of high inverted

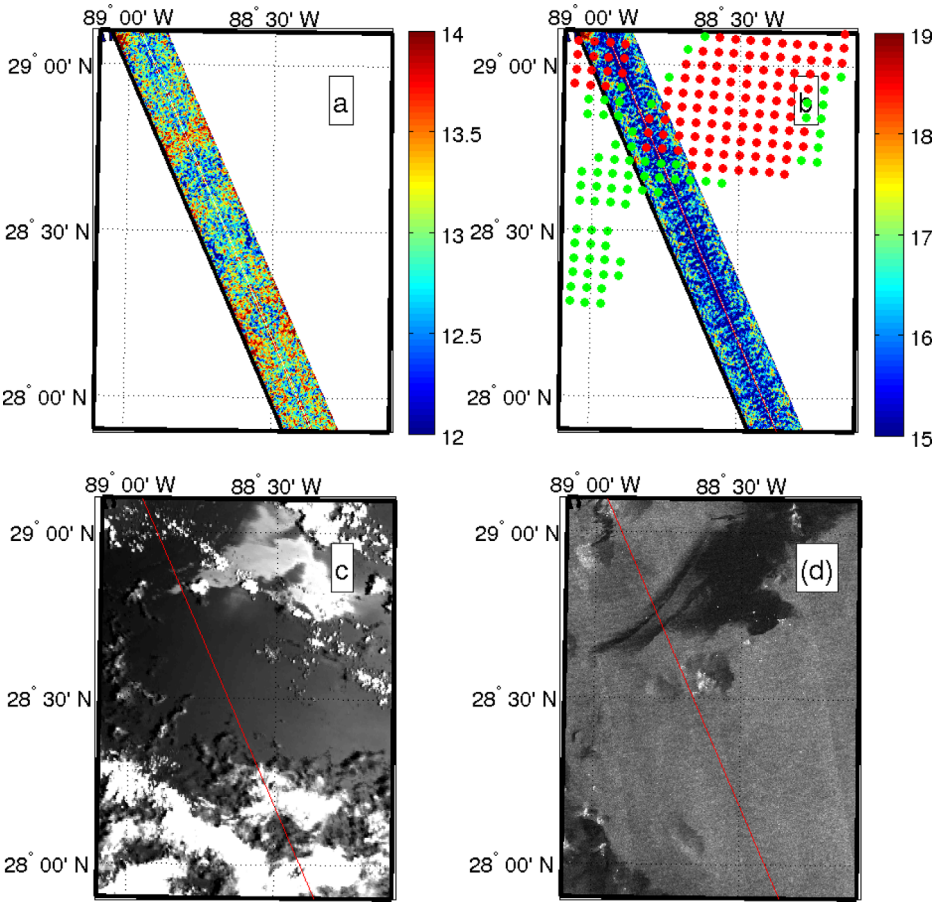

Figure 7. Inverted high-resolution (a) Ku-band and (b) C-band σ_0 (in dB) for Jason-2 pass 204 cycle 073 (3 July 2010 21:45 UTC). The green and red dots in Figure 7b represent the ERMA thin and thick oil cover respectively. (c) MODIS Terra image (4 July 2010 16:40 UTC). (d) Cosmo-Skymed-1 SAR image (3 July 2010 11:56 UTC).

Ku-band and C-band σ_0 (Figure 9b). However, compared to the SAR images and the ERMA analysis, the altimeter inverted σ_0 reveal the high variability at small scale of the surface backscatter within the oil-covered region. That is certainly associated with the thickness of oil, which is not well detected by SAR or visible images analysis.

3.3. Evolution of Inverted σ_0 During the Oil Spill

Using the method of inversion of waveform, we reprocess all the Jason-1 (pass 015) and Jason-2 (pass 204) altimeter data during the DWH spill to show the evolution of σ_0 during the oil spill. Figures 10a and 10b present the evolution of inverted Ku-band σ_0 for Jason-2 (from cycles 066 to 075) and Jason-1 (from cycles 306 to 314), respectively. For each cycle, the mean backscatter for the samples not covered by oil in the ERMA analysis has been subtracted to enhance the local impact of oil spill on backscatter. The red and white cross-hatched regions represent the collocated and coincident ERMA thick and thin oil covers within one day of altimeter measurements, respectively. The mean ECMWF and altimeter wind speed are also given in the figure. The rain flagged samples in the SGDR have been discarded from the analysis.

At low wind speed (<3 m s^{-1}), the presence of oil either thin or thick is always associated with strong local increase of surface backscatter as shown in Jason-2 cycles 67, 69, and 71, and Jason-1 cycles 310 and 312. Given the lower resolution and the uncertainties of the thickness analysis of the ERMA fields, thicker oil corresponds to larger σ_0 enhancement than that for thin oil. Locally, the σ_0 increase can exceed 10 dB. Within the oil-covered zones, the large σ_0 variation, i.e., the notable attenuation of surface roughness, reflects the variation of oil thickness. Compared with the ERMA analysis, the altimeters give a more detailed description of the oil thickness distribution.

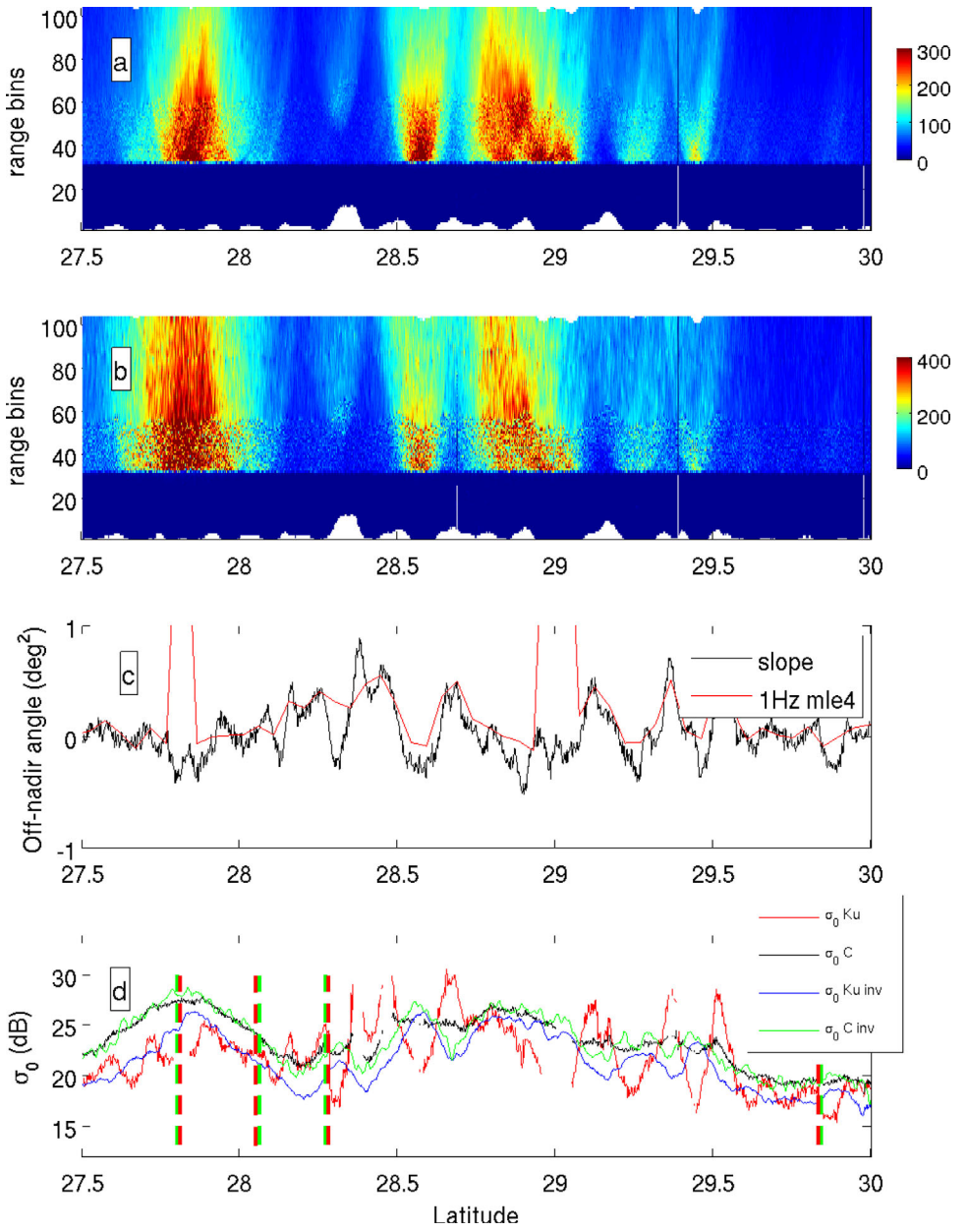

Figure 8. Repositioned Jason-1 (a) Ku-band and (b) C-band waveforms for pass 015 cycle 310 (1 June 2010 18:15 UTC). The color scale represents the linear backscatted waveform power. (c) Off-nadir angles from the 1 Hz MLE4 estimator (red line) and inferred from the waveforms plateau slope (black line). (d) Ku-band and C-band MLE-4 σ_0 (red and black lines) and mean along-track inverted Ku-band and C-band σ_0 (blue and green lines). The dashed green and red line represent the limits of the ERMA thin and thick oil cover within the altimeter swath.

At moderate winds (3–6 m s^{-1}), high agreement between oil cover and σ_0 increase is shown in Jason-2 cycles 70, 72, 74, and 75 and Jason-1 cycles 306, 309, 311, and 314. Although the σ_0 increase within the oil spill is more limited than that at low wind, it can still reach 2 dB. Moreover, the variation of the σ_0 is larger within thick oil cover than that within thin oil. At higher winds (larger than 6 m s^{-1}), for Jason-2 cycle 66, 68, and 73 and Jason-1 307, 308, 309, and 313, the effect of oil on the σ_0 is only detectable within thick oil for the Jason-1 cycles 307 and 208. The variation of σ_0 exceeds 1 dB where the oil thickness is large. For most cycles, the σ_0 variations induced by wind variability are of the same order of magnitude as the ones caused by the spill.

To quantify the effect of oil on surface backscatter, the mean inverted Ku-band and C-band σ_0 distributions computed as a function of ECMWF wind speed and ERMA oil cover are shown in Figures 11 and 12,

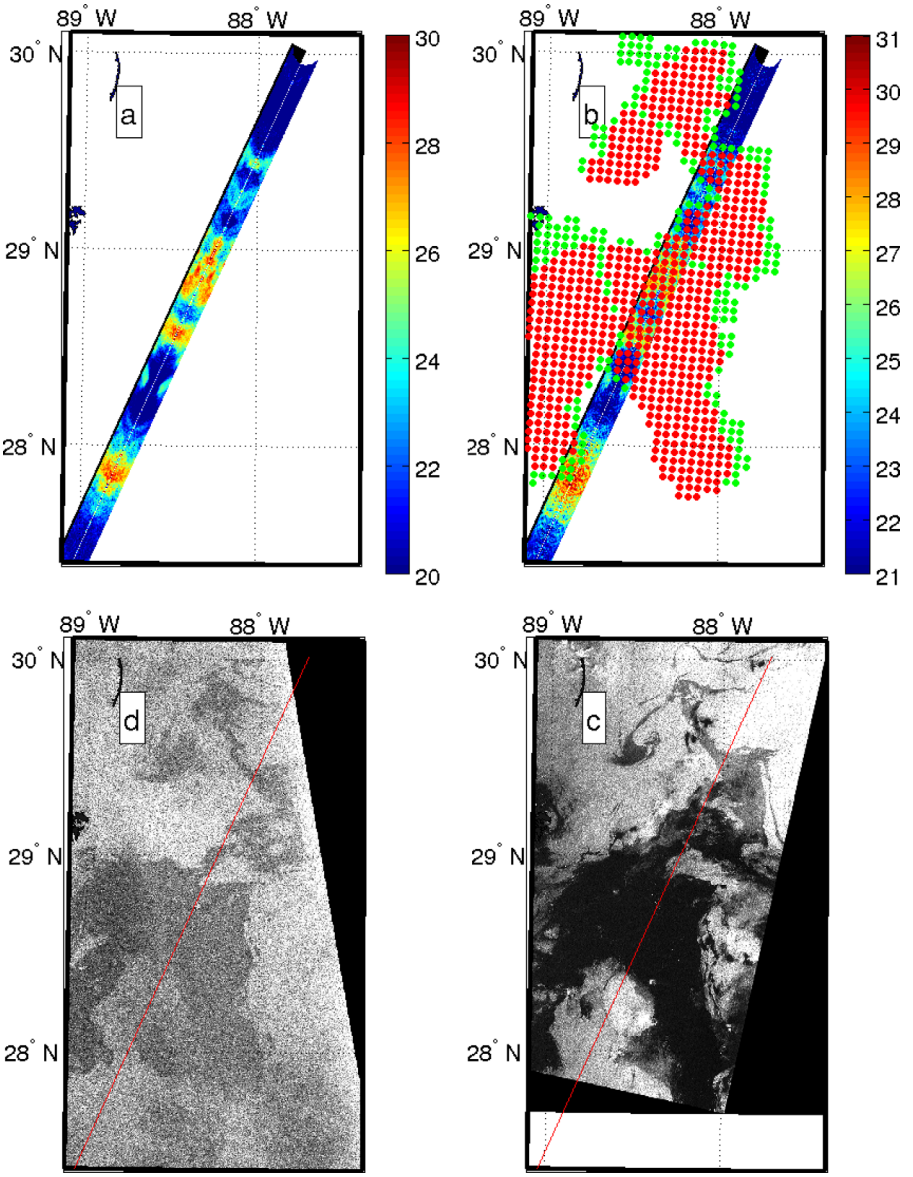

Figure 9. Inverted high-resolution (a) Ku-band and (b) C-band σ_0 (in dB) for Jason-1 pass 015 cycle 310 (1 June 2010 18:15 UTC). The green and red dots in Figure 9b represent the ERMA thin and thick oil cover respectively. (c) Radarsat-1 SAR image (1 June 2010 23:58:05 UTC). (d) Radarsat-2 SAR image (1 June 2010 12:01 UTC).

respectively. The means of σ_0 are listed in Table 1. The mean along-track σ_0 has been considered because its resolution is of the same order as the ERMA fields. At low wind speeds ($<$3 m s^{-1}), the distribution of σ_0 at both Jason-2 and Jason-1 Ku-band and C-band σ_0 (Figures (11 and 12)a, and 12d) are significantly shifted toward higher values for thick oil. The mean σ_0 increase is similar for both Ku and C bands in the order of 1.0–3.5 dB for thick oil (Table 1). For thin oil, the shift toward higher value is smaller than that for thick oil for both Ku and C bands in the order of 0.9–2.9 dB.

For moderate winds (3–6 m s^{-1}), (Figures 11 and 12b, and 12e), there is a clear shift of the Ku-band and C-band σ_0 distributions toward larger values, especially for associated with higher σ_0 increase at both Ku and C bands while the oil thickness has no significant impact on Jason-2 σ_0. At winds larger than 6 m s^{-1}, the Jason-1 and Jason-2 Ku-band σ_0 (Figures 11 and 12c, and 12f) distributions for thick oil are slightly shifted toward higher values with a mean increase of 0.2–0.5 dB while the C-band σ_0 is not affected. There is also no detectable impact of thin oil on Jason-1/2 Ku-band and C-band backscatter.

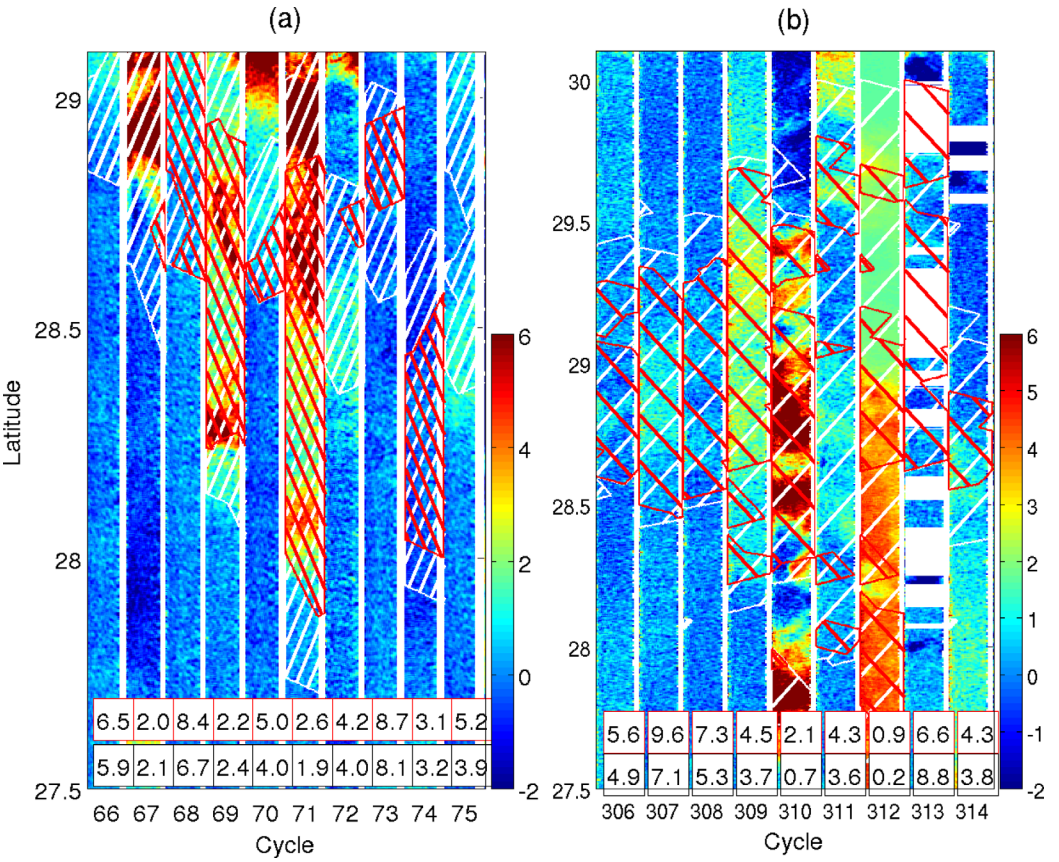

Figure 10. Inverted high-resolution Ku-band σ_0 (in dB). The mean σ_0 outside the oil spill has been subtracted from each cycle to enhance the impact of the oil spill. The coincident and collocated ERMA thick and thin oil spill cover within the altimeter swath are represented as red and white cross-hatching, respectively. The mean ECMWF and altimeter wind speeds (m s^{-1}) are given for each cycle in the first and second row respectively. (a) Jason-2 pass 204 and cycles 066–075 (every 10 days from 25 April 2010 to 24 July 2010). (b) Jason-1 pass 015 and cycles 306–314 (every 10 days from 23 April 2010 to 24 July 2010). The white zones correspond to rain flagged data.

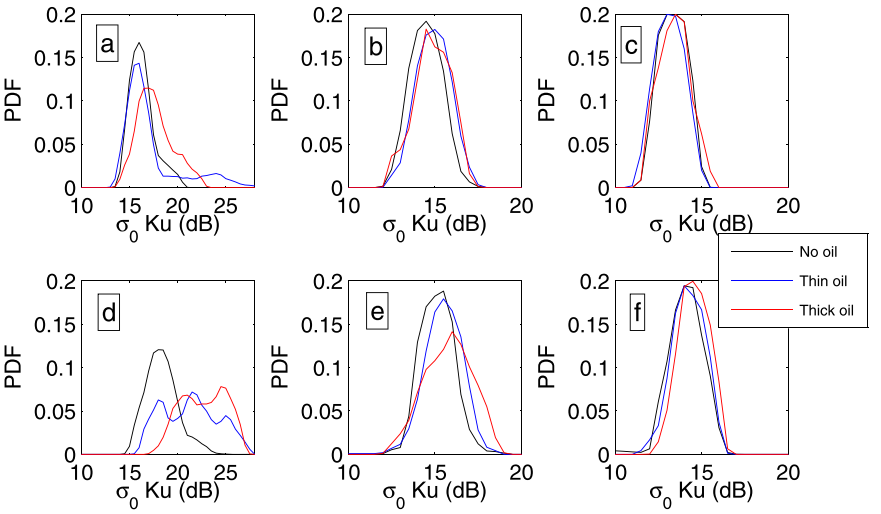

Figure 11. Histogram of Ku-band σ_0 for (a–c) Jason-2 pass 204 cycles 66–75 and (d–f) Jason-1 pass 015 cycle 306–314. The σ_0 is shown as a function of the oil cover and wind speed: wind $<$ 3 m s^{-1} (Figures 11a and 11d), 3 $<$ wind $<$ 6 m s^{-1} (Figures 11b and 11e), and wind $>$ 6 m s^{-1} (Figures 11c and 11f).

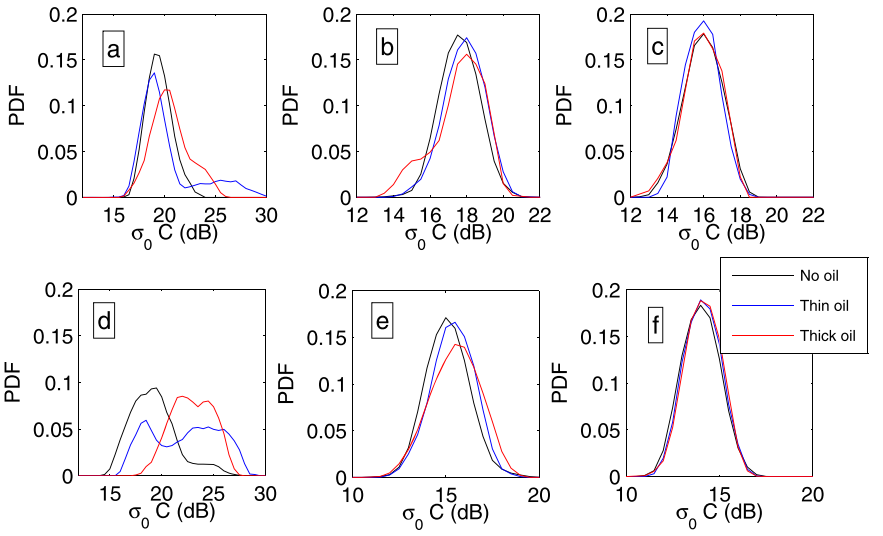

Figure 12. Histogram of C-band σ_0 for (a–c) Jason-2 pass 204 cycles 66–75 and (d–f) Jason-1 pass 015 cycle 306–314. The σ_0 is shown as a function of the oil cover and wind speed: wind <3 m s^{-1} (Figures 12a and 12d), $3<$ wind <6 m s^{-1} (Figures 12b and 12e), and wind >6 m s^{-1} (Figures 12c and 12f).

The off-nadir angle is a good estimator of the waveform distortion and the presence of strong inhomogeneity of surface backscatter within the altimeter footprint. The distributions and mean of the absolute value of the off-nadir angle as a function of wind speed and oil cover are presented in Figure 13 and Table 2. At low wind speeds, the distributions and the mean values imply that both Jason-1 and Jason-2 waveforms are notably distorted within oil-covered zones. For Jason-2, the mean off-nadir angle strongly increases from 0.032 deg^2 for no oil to 0.047 deg^2 and 0.064 deg^2 for thin and thick oil (see Table 2), indicating larger inhomogeneity of the surface backscatter. For Jason-1, the mean off-nadir angle increases from 0.069 deg^2 for no oil to 0.14 and 0.23 deg^2 for thin and thick oil. The bin averaging of the waveform plateau region and the associated higher noise level explains the higher sensitivity of Jason-1 to waveform distortion. Hence, the shift of off-nadir angle distribution for Jason-1 (Figure 13c) is more significant than that for Jason-2 (Figure 13a). At low wind, the sea surface short waves are small and the roughness is low. The surface backscatter is high and small variations of surface roughness translates into large variations of surface backscatter [*Kudryavtsev et al.*, 2012]. The presence of film on the surface leads to strong inhomogeneities of surface backscatter and thus high waveform distortion.

At moderate and higher winds, the impacts of oil thickness on Jason-1/2 off-nadir angle are similar with each other. For 3–6 m s^{-1} winds, Jason-2 (Jason-1) off-nadir angle increases from 0.015 (0.12) deg^2 to 0.025 (0.022) for thin oil and 0.027 (0.025) deg^2 for thick oil. Note that the mean off-nadir value even for thick oil is lower than that at low wind for oil free regions. When the wind increases, short wave grows and changes of surface roughness leads to smaller changes of surface backscatter and thus smaller inhomogeneity of the surface backscatter and smaller waveform distortion than that at low winds.

Table 1. Mean σ_0 (in dB) as a Function of Wind Speed and Oil Cover

	Ku Band			C Band		
Wind Speed	No Oil	Thin Oil	Thick Oil	No Oil	Thin Oil	Thick Oil
Jason-2						
0–3 m s^{-1}	16.3	17.2	17.7	19.5	20.3	20.6
3–6 m s^{-1}	14.5	14.9	14.9	17.6	17.9	17.6
>6 m s^{-1}	13.3	13.2	13.4	16.0	15.9	15.9
Jason-1						
0–3 m s^{-1}	18.4	21.3	22.7	19.3	22.2	22.9
3–6 m s^{-1}	15.1	15.5	15.8	15.1	15.3	15.5
>6 m s^{-1}	14.1	14.2	14.6	14.0	14.1	14.1

4. Discussion and Summary

Surface films of natural or artificial origin damp short wind waves [*Cox and Munk*, 1954]. This damping of the capillary and short gravity waves by surface film produces dark slick signatures in SAR imagery and large contrast in sun-glitter imagery, bright and dark depending upon the local solar geometry [*Hu et al.*, 2009; *Kudryavtsev et al.*, 2012]. For

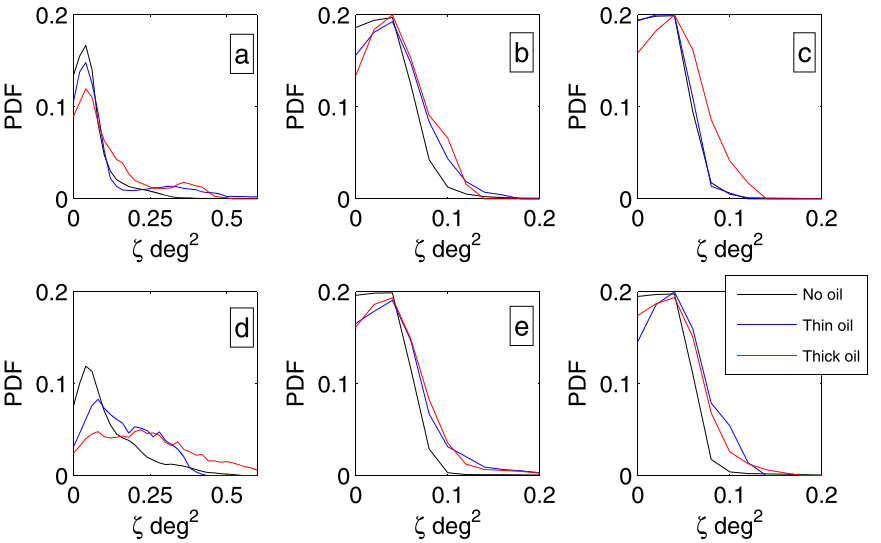

Figure 13. Histogram of off-nadir angle as a function of oil cover and wind speed for (a–c) Jason-2 pass 204 cycle 66–75 and (d–f) Jason-1 pass 015 cycle 306 to 314: wind < 3 m s^{-1} (Figures 13a and 12d), $3 <$ wind < 6 m s^{-1} (Figures 13b and 12e), and wind > 6 m s^{-1} (Figures 13c and 12f).

altimeter, specular reflection dominates and can produce bright patches or σ_0 bloom. Interpretation can follow the expected slope variance reduction [*Kudryavtsev et al*., 2005] based on *Ermakov et al*. [1992] surface slick elasticity model. Under light winds ($\leq$3 m s^{-1}), short gravity waves can be totally suppressed, resulting in σ_0 drops in SAR images and very large σ_0 increases at nadir in altimeter data [*Tournadre et al*., 2006]. At low winds, small changes of wind speed and/or surface film elasticity (i.e., oil thickness) translate into large variations of specular reflection at small scale (but little Bragg scattering variations), causing significant altimeter waveform distortion.

With wind increasing, the background sea surface roughness becomes more homogeneous and the altimeter waveforms are less distorted. Moreover, the damping of capillary waves by surface film decreases [*Kudryavtsev et al*., 2012]. At higher winds, only high elasticity films significantly dampen the shorter capillary waves and only is the Ku-band altimeter (i.e., the shorter capillary waves) significantly affected by film as it would require larger elasticity to dampen the longer C-band capillary waves.

Few studies focus on exploring the effect of oil slicks on satellite altimeter waveforms and σ_0. Lack of collocated and coincident information between oil spill and altimeter data limited the investigation to mainly theoretical modeling studies. Taking advantage of the large data set acquired during the DWH oil spill accident, we quantify the effect of oil slicks on altimeter data. The high-resolution σ_0 estimated by the waveform inversion method of *Tournadre et al*. [2011] is used to illustrate the effects of oil slick presence on surfaceσ_0. We collocated the Jason-1/2 altimetry data with SAR/MODIS imagery and ERMA oil cover data set to analyze the distortion of 20 Hz high-rate waveforms, surface σ_0 and off-nadir angle as a function of wind speed.

The σ_0 always increases within slicks, due to the attenuation of short surface waves by surface film. At low winds, both frequencies (Ku and C bands) of Jason-1 and 2 σ_0 distributions are shifted toward higher values in oil-covered regions and the shift is more pronounced for thicker oil (Figure 11a, 11d, 12a, and 12d). The increase of Ku-band and C-band σ_0 reaches 10 dB for thick oil (Figure 3). Jason-1/2 Ku-bands and C-bands show similar significant response to the thick oil (mean increase of 1.0–3.5 dB) and higher than that to thin oil (mean increase of 0.9–2.9 dB) (Table 1). Furthermore, the modulation of altimeter data

Table 2. Mean Off-Nadir Angle (in deg^2) as a Function of Wind Speed and Oil Cover

	Wind Speed	No Oil	Thin Oil	Thick Oil
Jason-2	0–3 m s^{-1}	0.032	0.047	0.064
	3–6 m s^{-1}	0.015	0.025	0.027
	>6 m s^{-1}	0.010	0.012	0.027
Jason-1	0–3 m s^{-1}	0.069	0.14	0.23
	3–6 m s^{-1}	0.012	0.022	0.025
	>6 m s^{-1}	0.012	0.024	0.021

appears to be significantly more sensitive to film thickness than those of SAR and visible data. With the increase of wind speed, the impact of oil on σ_0 decreases for both frequencies. The difference of the effects between thick and thin oil becomes less pronounced due to the uncertainties of oil thickness analysis from SAR and visible imagery. Under moderate wind, the effect of oil on Jason-1/2 Ku-band σ_0 reaches 2 dB and can still be of the order of 1 dB for winds larger than 6 m s^{-1} (Figure 10). With increasing winds, the impact of oil on C-band σ_0 becomes smaller than that at Ku band in good agreement with theoretical work by *Kudryavtsev et al*. [2012].

The analysis of the waveform distortion shows that at low winds, the off-nadir angle could be used as an additional factor to monitor the oil slicks and help the validation of oil thickness estimates. At moderate and higher winds, although the waveforms are more distorted within oil-covered regions, the values of the off-nadir angle are smaller than the one measured at low winds over oil free regions, which limits their potential use for spill detection.

Surface film causes σ_0 bloom in altimeter data and Jason-1/2 altimeter signal is more sensitive to oil thickness than SAR data. In short, altimeter data can certainly be used as a complementary data set to validate and delineate thick oil cover. The σ_0 inversion method throws a light on using airborne and satellite altimetry data for oil spill monitoring.

Appendix A: Altimeter Waveforms Inversion

The altimeter waveform inversion is described in detail in *Tournadre et al*. [2011] and is here summarized. Assuming that the distribution of the sea surface roughness and of the elevation are homogeneous over the altimeter footprint, the backscatter coefficient can be expressed as a convolution product of the radar point target response, the flat sea surface response and the joint probability density function of slope and elevation of the sea surface [*Brown*, 1977; *Barrick and Lipa*, 1985]. Further assuming that the altimeter antenna beam pattern g is a Gaussian of standard deviation u_b, that the compressed pulse P is also a Gaussian of standard deviation σ_τ and that the joint probability of sea surface slope and elevation p_j is Gaussian, the cross section σ is given by *Brown* [1977] and *Barrick and Lipa* [1985]

$$\sigma(t)=\frac{\pi^2 H''|R(0)|^2\sigma_\tau\sigma_0}{2\sigma_p}\int_0^{\infty} e^{-\frac{u}{u_b}}e^{-\frac{(x-u)^2}{2\sigma_p^2}}du \tag{A1}$$

where t is the time, $x=ct/2$ is the distance between the surface and the antenna, $u=\left(H'\psi^2\right)/2$ is the ground range, H' and H'', defined by $H'=H(1+H/a)$ and $H''=H/(1+H/a)$, are the reduced and extended satellite heights, H being the satellite altitude and a the earth's radius; $R(0)$ is the Fresnel coefficient at zero incidence, u_b is defined by $u_b=(H'\psi_b^2)/2$, with $\psi_b=\psi_H/\sqrt{8\ln 2}$, ψ_H being the two-way half-power antenna beam width. σ_p is defined by $\sigma_p=\sqrt{h^2+\sigma_\tau^2}$; h is the rms wave height and σ_0 is the mean surface backscatter coefficient defined as a function of the rms of the wave slopes (s_x and s_y) in two orthogonal directions and ρ_{xy} is the correlation coefficient of the wave slopes along this two axes by $\sigma_0=(2s_xs_y\sqrt{1-\rho_{xy}^2})^{-1}$.

Assuming that the wave height is homogeneous over the altimeter footprint and that σ_0 is modulated by short scale variations, the echo waveform (A1) becomes

$$\sigma_0(t)=\alpha\int_0^{2\pi}\int_0^{\infty}\sigma_s(u,\theta)e^{-\frac{u}{u_b}}e^{-\frac{(ct/2-u)^2}{2\sigma_p^2}}dud\theta \tag{A2}$$

where $\alpha=\frac{\pi^2H''|R(0)|^2\sigma_\tau}{2\sigma_p}$ is a normalization coefficient, θ is the azimuth, u is the range, c is the speed of light, and σ_s is the surface backscatter.

Let us consider a group of N measured waveforms w_i, and the surface σ_s on a regular grid $\{x_{kl},y_{kl}\}$, using equation (A2), the jth element of the ith waveform w_{ij} is can be expressed in a discrete form as the sum of the σ_{kl} whose range is between the range limits $\{u_j,u_{j+1}\}$ of bin j,

$$w_{ij}=\alpha\sum_k\sum_l a_{kl}\sigma_{kl}e^{-\frac{u(k,l)}{u_b}}\left(1+erf\left(\frac{u_j}{\sqrt{2}\sigma_p}\right)\right) \tag{A3}$$

where the range u_{kl} satisfies

$$u_j \le u_{kl} = \frac{(x_{kl}-x_i^0)^2+(y_{kl}-y_i^0)^2}{H'' c\tau} \le u_{j+1} \tag{A4}$$

where τ is the pulse length, x and y are the along and across track coordinates, x_i^0 and y_i^0 are the nadir coordinates of the ith waveform, and a_{kl} is the surface of the intersection of the $\{k, l\}$ grid cell and the annulus of bin j. In a first-order approximation, we assume all the u_{kl} to be equal to $\overline{u_j} = (u_j + u_{j+1})/2$, thus equation (A3) simplifies to

$$W_{ij} = w_{ij} \frac{e^{\frac{\overline{u_j}}{u_b}}}{\left(1+erf\left(\frac{\overline{u_j}}{\sqrt{2}\sigma_p}\right)\right)} = \alpha \sum_{k,l} a_{kl}\sigma_{kl} \tag{A5}$$

where W represents the waveform detrended for beam width by the term $e^{\frac{\overline{u_j}}{u_b}}$ and wave height effects by the term $\left(1+erf\left(\frac{\overline{u_j}}{\sqrt{2}\sigma_p}\right)\right)^{-1}$.

In a matrix form, the group of waveform $\{w_{ij},\ i=1..N, j=1..M\}$ is expressed as

$$\boldsymbol{W} = \boldsymbol{A}.\boldsymbol{S} \tag{A6}$$

where $\boldsymbol{S}$ is the matrix of the mean left/right surface backscatter (because of the left/right symmetry of the altimeter imaging process) and $\boldsymbol{A}$ is the altimeter imaging matrix that depends only on the altimeter geometry and can be easily computed using the range equation (A4). The imaging matrix can be easily computed by simple geometry. Let X_{ij} be a surface grid element of area dx, dy centered on x_{ij}, y_{ij}. The coefficient a_{ijkl} of the imaging matrix A is equal to the surface of intersection between the grid element and the annulus centered at x_0^k, y_0^k and radii r_l and r_{l+1} (i.e., the range of bin l).

$$a_{ijkl} = \int_{y_{ij}-\frac{dy}{2}}^{y_{ij}+\frac{dy}{2}} [f_1(y) - f_2(y)]dy \tag{A7}$$

where

$$f_1(y) = \min\left(\sqrt{r_{l+1}^2-(y-y_0^k)^2}, x_{ij}+\frac{dx}{2}\right) \tag{A8}$$

$$f_2(y) = \max\left(\sqrt{r_l^2-(y-y_0^k)^2}, x_{ij}-\frac{dx}{2}\right) \tag{A9}$$

where

$$r_l = \sqrt{lH'' c\tau} \tag{A10}$$

The resolution of the surface backscatter grid has been chosen as the distance between two consecutive HR waveforms (290 m for Jason). The minimum number of waveforms to be considered is constrained by the width of the image of a nadir point in the waveform space that is about 3 seconds of data or 60 waveforms. In practice, N has been fixed to 75. For such grids, the linear system of equations (A6) is overdetermined and can be inverted using pseudo-Moore-Penrose inverse $\boldsymbol{A}^+$ computed using singular value decomposition [*Penrose*, 1955].

$$\boldsymbol{S} = \boldsymbol{A}.^+\boldsymbol{W} \tag{A11}$$

Acknowledgments

This work was partly supported by the National Key Research and Development Program of China, China (2016YFC1401905), National Natural Science Foundation of China, China (grants 41306194), and the Old Dominion University's Climate Change and Sea Level Rise Initiative (CCSLRI). The Jason-1 and Jason-2 data are available at http://www.aviso.altimetry.fr. National Aeronautics and Space Administration's (NASA) Gulf Oil Spill Data are available at http://gulfoilspill.jpl.nasa.gov. Environmental Response Management Application (ERMA) archive oil spill data are downloaded from https://gomex.erma.noaa.gov/. The SAR/MODIS images are collected by the Center For Southeastern Tropical Advanced Remote Sensing (CSTARS), Rosenstiel School of Marine and Atmospheric Science, U. Miami (https://www.cstars.miami.edu/cstars-projects/deepwaterhorizon/). We are thankful to the reviewers for their constructive comments and suggestions. The views, opinions, and findings contained in this report are those of the authors and should not be construed as an official NOAA or U.S. Government position, policy, or decision.

References

Bao, S., X. Li, D. Shen, Z. Yang, L. J. Pietrafesa, and W. Zheng, (2016), Ocean upwelling along the Yellow Sea coast of China revealed by satellite observations and numerical simulation, *IEEE Trans. Geosci. Remote Sens.*, *55*, 526–536, doi:10.1109/TGRS.2016.2610761.

Barrick, D., and B. Lipa (1985), Analysis and interpretation of altimeter sea echo, *Adv. Geophys.*, *27*, 61–100.

Brown, G. S. (1977), The average impulse response of a rough surface and its applications, *IEEE Trans. Antennas Propag.*, *25*(1), 67–74.

Bulgarelli, B., and S. Djavidnia (2012), On MODIS retrieval of oil spill spectral properties in the marine environment, *IEEE Geosci. Remote Sens. Lett.*, *9*(3), 398–402.

Buono, A., F. Nunziata, M. Migliaccio, and X. Li (2016), Polarimetric analysis of compact-polarimetry SAR architectures for sea oil slick observation, *IEEE Trans. Geosci. Remote Sens.*, *54*(10), 5862–5874, doi:10.1109/TGRS.2016.2574561.

Caruso, M. J., M. Migliaccio, J. T. Hargrove, O. Garcia-Pineda, and H. C. Graber (2013), Oil spills and slicks imaged by Synthetic Aperture Radar, *Oceanography*, *26*(2), 112–123.

Chelton, D. E., J. C. Ries, B. J. Haines, L.-L. Fu, and P. S. Callahan (2001), *Satellite Altimetry and Earth Sciences*, chap. 1, Academic, San Diego, Calif.

Cheng, Y., X. Li, Q. Xu, O. B. Andersen, and W. G. Pichel (2011), SAR observation and model tracking of an oil spill event in coastal waters, *Mar. Pollut. Bull.*, *62*(2), 350–363.
Cheng, Y., B. Liu, X. Li, F. Nunziata, Q. Xu, X. Ding, M. Migliaccio, and W.G. Pichel (2014), Monitoring of oil spill trajectories with COSMO-SkyMed X-Band SAR images and model simulation, *IEEE J. Selec. Top. Appl. Earth Obs. Remote Sens.*, *7*(7), 2895–2901.
Cox, C., and W. Munk (1954), Measurement of the roughness of the sea surface from photographs of the sun's glitter, *J. Opt. Soc.*, *44*(11), 838–850.
Crone, T. J., and M. Tolstoy (2010), Magnitude of the 2010 Gulf of Mexico oil leak, *Science*, *330*(6004), 634–634.
Ermakov, S., S. Salashin, and A. Panchenko (1992), Film slicks on the sea surface and some mechanisms of their formation, *Dyn. Atmos. Oceans*, *16*, 279–304.
Fingas, M., and C. Brown (2014), Review of oil spill remote sensing, *Mar. Pollut. Bull.*, *83*(1), 9–23.
Fiscella, B., A. Giancaspro, F. Nirchio, P. Pavese, and P. Trivero (2000), Oil spill detection using marine SAR images, *Int. J. Remote Sens.*, *21*(18), 3561–3566.
Gade, M., W. Alpers, H. Hühnerfuss, and P. A. Lange (1998a), Wind wave tank measurements of wave damping and radar cross sections in the presence of monomolecular surface films, *J. Geophys. Res.*, *103*(C2), 3167–3178.
Gade, M., W. Alpers, H. Hühnerfuss, H. Masuko, and T. Kobayashi (1998b), Imaging of biogenic and anthropogenic ocean surface films by the multifrequency/multipolarization SIR-C/X-SAR, *J. Geophys. Res.*, *103*(C9), 18,851–18,866.
Garcia, A. (1999), Study of the origins of the sigma0 blooms, master's thesis, 159 pp., Dept. of Electr. and Comput. Eng., Va. Polytech. Inst. and State Univ., Blacksburg.
Garcia-Pineda, O., I. R. MacDonald, X. Li, C. R. Jackson, and W. G. Pichel (2013), Oil spill mapping and measurement in the Gulf of Mexico with Textural Classifier Neural Network Algorithm (TCNNA), *IEEE J. Selec. Top. Appl. Earth Obs. Remote Sens.*, *6*(6), 2517–2525.
Hu, C., X. Li, W. G. Pichel, and F. E. Muller-Karger (2009), Detection of natural oil slicks in the NW Gulf of Mexico using MODIS imagery, *Geophys. Res. Lett.*, *36*, L01604, doi:10.1029/2008GL036119.
Jones, C. E., B. B. Minchew, B. B. Holt, and S. S. Hensley (2011), Studies of the *Deepwater Horizon* oil spill with the UAVSAR radar, in *Monitoring and Modeling the Deepwater Horizon Oil Spill: A Record-Breaking Enterprise*, pp. 33–50, AGU, Washington, D. C.
Kim, T., K. Park, X. Li, M. Lee, S. Hong, S. Lyu, and S. Nam (2015), Detection of the Hebei Spirit oil spill on SAR imagery and its temporal evolution in a coastal region of the Yellow Sea, *Adv. Space Res.*, *56*(6), 1079–1093, doi:10.1016/j.asr.2015.05.040.
Kourafalou, V. H., and Y. S. Androulidakis (2013), Influence of Mississippi River induced circulation on the Deepwater Horizon oil spill transport, *J. Geophys. Res. Oceans*, *118*, 3823–3842, doi:10.1002/jgrc.20272.
Kudryavtsev, V., D. Akimov, J. Johannessen, and B. Chapron (2005), On radar imaging of current features: 1. Model and comparison with observations, *J. Geophys. Res.*, *110*, C07016, doi:10.1029/2004JC002505.
Kudryavtsev, V., A. Myasoedov, B. Chapron, J. A. Johannessen, and F. Collard (2012), Joint sun-glitter and radar imagery of surface slicks, *Remote Sens. Environ.*, *120*, 123–132, doi:10.1016/j.rse.2011.06.029.
Leifer, I., et al. (2012), State of the art satellite and airborne marine oil spill remote sensing: Application to the BP Deepwater Horizon oil spill, *Remote Sens. Environ.*, *124*, 185–209.
Li, X., X. Li, and M. X. He (2009), Coastal upwelling observed by multi-satellite sensors, *Sci. China Ser. D*, *52*(7), 1030–1038.
Li, X., C. Li, Z. Yang, and W. Pichel (2013), SAR imaging of ocean surface oil seep trajectories induced by near inertial oscillation, *Remote Sens. Environ.*, *130*, 182–187.
Liu, P., C. F. Zhao, X. Li, M. X. He, and W. Pichel (2010), Identification of ocean oil spills in SAR imagery based on fuzzy logic algorithm, *Int. J. Remote Sens.*, *31*(17–18), 4819–4833.
Liu, P., X. Li, J. J. Qu, W. Wang, C. Zhao, and W. Pichel (2011), Oil spill detection with fully polarimetric UAVSAR data, *Mar. Pollut. Bull.*, *62*(12), 2611–2618.
Liu, Y., A. MacFadyen, Z. G. Ji, and R. H. Weisberg (2013), *Monitoring and Modeling the Deepwater Horizon Oil Spill: A Record Breaking Enterprise*, vol. 195, John Wiley, Hoboken, N. J.
McNutt, M. K., R. Camilli, G. D. Guthrie, P. A. Hsieh, V. F. Labson, W. J. Lehr, D. Maclay, A. C. Ratzel, and M. K. Sogge (2011), *Assessment of Flow Rate Estimates for the Deepwater Horizon/Macondo Well Oil Spill*, Flow Rate Technical Group Report to the National Incident Command, Interagency Solutions Group, 30 pp., 10 Mar.
Migliaccio, M., and F. Nunziata (2014), On the exploitation of polarimetric SAR data to map damping properties of the Deepwater Horizon oil spill, *Int. J. Remote Sens.*, *35*(10), 3499–3519.
Minchew, B., C. E. Jones, and B. Holt (2012), Polarimetric analysis of backscatter from the Deepwater Horizon oil spill using L-band Synthetic Aperture Radar, *IEEE Trans. Geosci. Remote Sens.*, *50*(10), 3812–3830.
Mitchum, G., D. Hancock, G. Hayne, and D. Vandemark (2004), Blooms of sigma0 in the TOPEX radar altimeter data, *J. Atmos. Oceanic Technol.*, *21*, 1232–1245.
Nunziata, F., M. Migliaccio, and X. Li (2015), Sea oil slick observation using hybrid-polarity SAR architecture, *IEEE J. Oceanic Eng.*, *40*(2), 426–440, doi:10.1109/JOE.2014.2329424.
Penrose, R. (1955), A generalized inverse for matrices, *Proc. Cambridge Philos. Soc.*, *51*, 406–413.
Roesler, C. J., W. Emery, and S. Kim (2013), Evaluating the use of high-frequency radar coastal currents to correct satellite altimetry, *J. Geophys. Res. Oceans*, *118*, 3240–3259, doi:10.1002/jgrc.20220.
Sun, S., C. Hu, L. Feng, G. A. Swayze, J. Holmes, G. Graettinger, I. MacDonald, O. Garcia, and I. Leifer (2016), Oil slick morphology derived from AVIRIS measurements of the Deepwater Horizon oil spill: Implications for spatial resolution requirements of remote sensors, *Mar. Pollut. Bull.*, *103*(1), 276–285.
Thibaut, P., L. Amarouche, O. Z. Zanife, N. Steunou, P. Vincent, and P. Raizonville (2004), Jason-1 altimeter ground processing look-up Correction tables, *Mar. Geod.*, *27*(3–4), 409–431, doi:10.1080/01490410490902133.
Thibaut, P., F. Ferreira, and P. Femenias (2007), Sigma0 bloom events in the Envisat radar altimeter data, paper presented at Envisat Symposium 2007, vol. ESA SP-636, Eur. Space Agency, Montreux, Switzerland, 23–27 April.
Tournadre, J., B. Chapron, N. Reul, and D. C. Vandemark (2006), A satellite altimeter model for ocean slick detection, *J. Geophys. Res.*, *111*, C04004, doi:10.1029/2005JC003109.
Tournadre, J., J. Lambin-Artru, and N. Steunou (2009), Cloud and rain effects on AltiKa/SARAL Ka-band radar altimeter—Part II: Definition of a rain/cloud flag, *IEEE Trans. Geosci. Remote Sens.*, *47*(6), 1818–1826, doi:10.1109/TGRS.2008.2010127.
Tournadre, J., B. Chapron, and N. Reul (2011), High-resolution imaging of the ocean surface backscatter by inversion of altimeter waveforms, *J. Atmos. Oceanic Technol.*, *28*(8), 1050–1062.
Xu, Q., X. Li, Y. Wei, Z. Tang, Y. Cheng, and W. G. Pichel (2013), Satellite observations and modeling of oil spill trajectories in the Bohai Sea, *Mar. Pollut. Bull.*, *71*(1), 107–116.

Xu, Q., Y. Cheng, B. Liu, and Y. Wei (2015), Modeling of oil spill beaching along the coast of the Bohai Sea, China, *Frontiers Earth Sci.*, *9*(4), 637–641, doi:10.1007/s11707-015-0515-6.

Zhang, B., W. Perrie, X. Li, and W. G. Pichel (2011), Mapping sea surface oil slicks using RADARSAT-2 quad-polarization SAR image, *Geophys. Res. Lett.*, *38*, L10602, doi:10.1029/2011GL047013.

Zhang, B., X. Li, W. Perrie, and O. Garcia-Pineda (2017), Compact polarimetric synthetic aperture radar for marine oil platform and slick detection, *IEEE Trans. Geosci. Remote Sens.*, *55*(3), 1407–1423, doi:10.1109/TGRS.2016.2623809.

Zhao, J., M. Temimi, H. Ghedira, and C. Hu (2014), Exploring the potential of optical remote sensing for oil spill detection in shallow coastal waters—A case study in the Arabian Gulf, *Opt. Express*, *22*(11), 13,755–13,772.